



## *In situ* determination of the nanostructure effects on the activity, stability and selectivity of Pt-Sn ethanol oxidation catalysts



Laura Calvillo<sup>a,b,\*</sup>, Lucila Mendez De Leo<sup>c</sup>, Stephen J. Thompson<sup>a</sup>, Stephen W.T. Price<sup>a,d</sup>, Ernesto J. Calvo<sup>c</sup>, Andrea E. Russell<sup>a,\*\*</sup>

<sup>a</sup> Chemistry, University of Southampton, Highfield, Southampton SO17 1BJ, UK

<sup>b</sup> Dipartimento di Scienze Chimiche, Università di Padova, Via Marzolo 1, 35131 Padova, Italy

<sup>c</sup> INQUIMAE, Departamento de Química Inorgánica, Analítica y Química Física, Facultad de Ciencias Exactas y Naturales, Universidad de Buenos Aires, Argentina

<sup>d</sup> Diamond Light Source Ltd., Harwell Science and Innovation Campus, Didcot OX11 0DE, UK

### ARTICLE INFO

#### Keywords:

Pt-Sn nanostructures  
Ethanol electrooxidation  
*In situ* FTIRS  
*In situ* XAFS  
Structural stability

### ABSTRACT

Nanoparticle catalysts comprising two PtSn alloys with different Pt:Sn atomic ratios and a Sn modified Pt catalyst were prepared in order to study the effect of the particle nanostructures on the activity towards the ethanol electrooxidation and the selectivity to CO<sub>2</sub>. An accurate model of the electronic and structural properties, obtained by *ex situ* analysis, was established. Alloying of Sn with Pt causes the expansion of the lattice parameter of Pt and modifies its electronic structure. In contrast, the deposition of Sn on the Pt surface has neither effect. The activity of the catalysts towards ethanol oxidation was established voltammetrically and the CO<sub>2</sub> selectivity via *in situ* Fourier transform infrared spectroscopy (FTIRS). Results indicated that the modification of the electronic environment of Pt in Pt-Sn alloys results in a weaker adsorption of the intermediates (acetaldehyde and acetic acid), which desorb easily from the surface of the catalyst resulting in incomplete oxidation to CO<sub>2</sub>. In contrast, when the electronic structure is not perturbed (Sn modified Pt sample), the amount of CO<sub>2</sub> produced increases. The stability of the different nanostructures under working conditions was investigated by *in situ* X-ray absorption spectroscopy (XAS) measurements, which show that initially both the Sn modified Pt and Pt-Sn alloy nanostructures are stable under applied potential in the potential window studied and in presence of ethanol. Accelerated aging studies showed that the Sn modified Pt nanostructure remained stable, whereas a significant structural change was observed for the Pt-Sn alloys.

### 1. Introduction

The design of catalysts that are able to completely oxidize ethanol to CO<sub>2</sub> is an ongoing research challenge. Ethanol contains a C–C bond that is necessary to break in order to achieve its complete oxidation. The interest in the ethanol oxidation reaction (EOR) comes from the fact that the use of ethanol as fuel in direct ethanol fuel cells (DEFCs) makes these devices very promising for energy conversion, having the advantages of easier handling, storage and transport of the fuel than gaseous hydrogen [1]. Their use becomes even more advantageous when bioethanol produced from waste biomass is used as a sustainable source of the fuel.

Ethanol is difficult to oxidize on platinum or platinum alloys supported on carbon materials, which constitute the most common catalysts for DEFCs. Binary and ternary platinum-based catalysts have been tested as electrode materials, but the efficiency and/or durability of

systems operating with these catalysts is still insufficient for more demanding practical applications, especially at low temperatures. The overall efficiency of Pt-based electrocatalysts suffers the consequences of effective catalyst poisoning by CO that is an intermediate of the oxidation of any alcohol [2,3]. In order to minimize the poisoning effects and to increase the electrocatalytic activity, they are usually modified with oxophilic metals such as Ru, Sn, Mo, or Rh [4,5,6]. Using these catalysts, however, results in high yields of partial oxidation products like acetaldehyde and acetic acid, releasing two and four electrons per ethanol molecule, respectively, and hence generating lower energy conversion efficiency.

The binary Pt-Sn and ternary Pt-Rh-Sn catalysts are generally considered as the most effective ethanol oxidation reaction (EOR) catalysts [6,7,8]. Nevertheless, the origin of the promotion effect due to the presence of Sn in the ethanol oxidation in acidic media is still under debate and contradictions are found in the literature. There seems to be

\* Correspondence to: L. Calvillo, Dipartimento di Scienze Chimiche, Università di Padova, Via Marzolo 1, 35131 Padova, Italy.

\*\* Corresponding author.

E-mail addresses: [laura.calvillolamana@unipd.it](mailto:laura.calvillolamana@unipd.it) (L. Calvillo), [a.e.russell@soton.ac.uk](mailto:a.e.russell@soton.ac.uk) (A.E. Russell).

an agreement about the positive effect of Sn on the electrooxidation of CO due to its capacity to activate water at lower potentials than Pt, providing  $\text{OH}_{\text{ads}}$  species that help to oxidize the  $\text{CO}_{\text{ads}}$  [9,10,11]. However, contradictory results are reported about the ethanol electrooxidation, which may be explained by the different Pt:Sn ratio and Pt-Sn crystal structures used in these studies and/or by the extent of Pt:Sn alloying/mixing. For example, López-Suarez et al. state that the oxidation state of Sn, the Pt-Sn alloy formation and the Pt:Sn atomic ratio have a minimal influence on the catalytic activity of PtSn/C materials [12]; whereas Du et al. affirm that the Pt:Sn atomic ratio and the crystalline structure of Sn play an important role in the selectivity to  $\text{CO}_2$  [13].

Studies have shown that shape, structure, composition, and architecture are extremely important parameters [14,15], which affect catalytic activities of bimetallic nanostructured materials. Therefore, in order to design more efficient electrocatalysts, further understanding of the effects that the addition of other metals has on the Pt properties as well as relating these effects to catalytic activity, selectivity, and stability is needed. This requires the use of *in situ* techniques to investigate the dependence of the product distribution with the applied potential and to determine *in situ* structural changes induced by the applied electrochemical conditions [16].

In this work, we have prepared carbon supported Pt-Sn catalysts with different nanostructures, establishing an accurate model of the electronic and structural properties of each nanostructure using *ex situ* characterization techniques and verifying that the structures are retained in the electrochemical environment and in the presence of ethanol using *in situ* characterization techniques. The EOR activity of each catalyst has been measured using both thin film electrode studies and *in situ* FTIRS in order to determine the products obtained. This combined approach enables structure/property relationships to be defined. Finally, the structures of the catalysts, fresh and after potential cycling, have been studied using *in situ* XAS, providing the first such comprehensive characterization of both the initial state of the PtSn nanostructures as well as their long-term structural stability.

## 2. Experimental

### 2.1. Synthesis of catalysts and preparation of electrodes

#### 2.1.1. Sn modified Pt supported on carbon

The commercial 20 wt% Pt/C catalyst from Johnson Matthey, labelled as Pt/C-JM, was modified with one monolayer of Sn. 27.7 mg of  $\text{SnCl}_2 \cdot 2\text{H}_2\text{O}$  were dissolved in 30 mL of ultrapure water and subsequently added dropwise under sonication to a Pt/C-JM dispersion, which was prepared by the dissolution of 300 mg of Pt/C-JM catalyst in 30 mL of ultrapure water. After 30 min, an aqueous solution of  $\text{NaBH}_4$  (Sigma Aldrich, 9.3 mg of  $\text{NaBH}_4$  in 40 mL of ultrapure water) was added to the mixture dropwise under sonication. Once the addition of  $\text{NaBH}_4$  was completed, the mixture was stirred for 1 h at room temperature and, finally, the catalyst was filtered, washed with ultrapure water and dried overnight. This Sn modified Pt/C catalyst is labelled as Sn/Pt/C.

#### 2.1.2. Pt-Sn alloy supported on carbon

Two Pt-Sn alloys supported on carbon were prepared by the polyol method [17], using  $\text{H}_2\text{PtCl}_6$  (8 wt%, Sigma-Aldrich) and  $\text{SnCl}_2 \cdot 2\text{H}_2\text{O}$  (Sigma Aldrich) as metal precursors. The synthesis process involved the dissolution of both metal precursors in 60 mL of ethylene glycol (EG) under sonication conditions. The amount of each of the metal precursors was that necessary to obtain Pt:Sn atomic ratios of 3:1 and 1:1 and a total metal loading of 20 wt%. Then, the pH was adjusted to 11 using a 1 M NaOH solution (in EG) and 240 mg of carbon (Vulcan XC-72R) was added and maintained under sonication for 15 min. Subsequently, the system was refluxed at 195 °C for 2 h and then quickly cooled in a cold water bath. Finally, the catalysts were filtered, washed

with ultrapure water and dried overnight. The materials obtained are labelled as  $\text{Pt}_3\text{Sn}_1/\text{C}$  and  $\text{Pt}_1\text{Sn}_1/\text{C}$ .

#### 2.1.3. Electrodes

Electrodes of the Pt-Sn catalyst materials were manufactured by painting Nafion-based inks on to carbon paper (TGP-H-60) with a final Pt loading of 0.6 mg Pt  $\text{cm}^{-2}$ . The catalyst inks were prepared by dispersing the catalyst in a mixture of water and Nafion® (10.85 wt% solids in water, Johnson Matthey). The electrodes were then pressed at 180 °C and 1 bar for 3 min. Circular button electrodes of 1.25  $\text{cm}^2$  area were cut and hydrated in ultra-pure (Purite, 18 MΩ cm) boiling water before their use.

### 2.2. Physicochemical characterization

The bulk composition analysis was performed by an energy dispersive spectroscopy (EDX) probe attached to a Philips XL-30 ESEM microscope.

Transmission electron microscopy (TEM) was carried out on a JEOL JEM 2100 LaB6 microscope operating at 200 kV, conducted at the Research Complex at the Harwell Campus, UK. In addition, STEM-HAADF images for the Sn/Pt/C and  $\text{Pt}_3\text{Sn}_1/\text{C}$  catalysts were obtained using a Titan FEI with Cs probe-corrected (1 Å) at the “Laboratorio de Microscopias Avanzadas” at “Instituto de Nanociencia de Aragón - Universidad de Zaragoza”. Energy dispersive X-ray spectroscopy (EDS) measurements with a resolution of 5 eV/channel were recorded in order to obtain the composition profiles for Pt and Sn along the metal nanoparticles.

X-ray diffraction (XRD) patterns were recorded using a SuperNova Dual Wavelength diffractometer with  $\theta$ - $\theta$  configuration and operating with Cu K $\alpha$  radiation ( $\lambda = 0.15406$  nm) generated at 45 kV and 40 nm. The mean crystallite size along the c direction ( $L_c$ ) of the metal crystallites was calculated using the Scherrer equation with a value of  $k = 0.9$  using the Pt(220) width peak around  $2\theta = 70^\circ$  to avoid the influence of the broad band of the carbon support at  $2\theta \sim 25^\circ$  [18,19,20,21]. The (220) peak was also used to determine the lattice parameter, assuming the Pt fcc structure. From the values of the lattice parameter, the atomic fraction of Sn in the Pt-Sn alloys were calculated, assuming that the Pt-Sn lattice parameter follows Vegard's law and that the dependence of the lattice parameter on Sn content is the same for supported and unsupported Pt:  $\chi_{\text{Sn}} = (l_{\text{PtSn}} - l_{\text{Pt}})/0.352$ , where  $l_{\text{PtSn}}$  and  $l_{\text{Pt}}$  are the lattice parameters for the Pt-Sn/C and Pt/C, respectively. Using these values, the amount of Sn alloyed ( $\text{Sn}_{\text{al}}$ ) was calculated from the relation:  $\text{Sn}_{\text{al}} = \chi_{\text{Sn}} / [(1 - \chi_{\text{Sn}})(\text{Sn}/\text{Pt})_{\text{at}}]$ , being  $(\text{Sn}/\text{Pt})_{\text{at}}$  the nominal Sn/Pt atomic ratio.

X-ray photoelectron spectra (XPS) were acquired with an ESCAPUS Omicron spectrometer fitted with a Mg K $\alpha$  (1253.6 eV) 150 W X-ray source. Data processing was performed with XPSPEAK software to determine the chemical states of Pt and Sn and the surface composition of Pt-Sn nanoparticles. The background was corrected using the Shirley method, and the binding energy of C 1s peak from the support at 284.5 eV was taken as an internal standard. The Pt:Sn surface atomic ratio was calculated from the Pt 4f and Sn 3d peak areas taking into account the corresponding sensitivity factors.

### 2.3. Electrochemical characterization

A systematic study applying conventional electrochemical techniques (cyclic voltammetry and CO-stripping voltammetry) was performed in order to determine the efficiency of the catalysts in the ethanol oxidation reaction (EOR). The electrochemical measurements were conducted in a standard three-electrode electrochemical cell. Pt gauze was used as counter electrode and a Hg/Hg $_2\text{SO}_4$  electrode (MMS, calibrated as +0.695 V vs. RHE) placed inside a Luggin capillary was used as reference electrode. All the potentials in the text are referred to the reversible hydrogen electrode (RHE). A 0.5 M  $\text{H}_2\text{SO}_4$  solution,

prepared from high purity reagents (Fisher Scientific) and purged with nitrogen gas, was used as supporting electrolyte. All the electrochemical experiments were carried out at room temperature. The oxidation of ethanol was studied by cyclic voltammetry. 1 M CH<sub>3</sub>CH<sub>2</sub>OH in 0.5 M H<sub>2</sub>SO<sub>4</sub> solution was used to carry out the experiments. Cyclic voltammetry experiments between 0.05 and 0.7 V vs. RHE were performed. Ten conditioning scans at 0.1 V s<sup>-1</sup> were initially performed in order to get a good contact between the electrode and electrolyte and, subsequently, three more cyclic voltammograms were measured at 0.02 V s<sup>-1</sup>. The third CV was used for comparison of the performance of the different catalysts towards the ethanol electrooxidation. The currents shown in the text are normalized by the electrochemical active surface area (specific activity) determined by monitoring the complete elimination of a CO adsorbed monolayer (CO stripping), assuming a charge of 420 μC cm<sup>-2</sup> involved in the oxidation of a monolayer of linearly adsorbed CO. The procedure for the CO stripping measurements is detailed in the Supplementary Information (SI).

The samples were subjected to an accelerated aging treatment (AAT) in order to study the stability of the nanostructures with time. They consisted of 1000 cycles between 0.05 and 0.6 V in 0.5 M H<sub>2</sub>SO<sub>4</sub> at 60 °C using a scan rate of 0.05 V s<sup>-1</sup>.

#### 2.4. *In situ* X-ray absorption measurements

An *in situ* electrochemical cell was used to collect EXAFS data of the Pt-Sn/C catalysts as a function of potential [22]. The working electrode was held in place by an Au wire contact, a Pt wire served as the counter electrode, and the reference electrode was a mercury mercurous sulfate (Hg/Hg<sub>2</sub>SO<sub>4</sub>) electrode that was connected to the cell *via* a short length of tubing containing the electrolyte. The cell was controlled by an Autolab potentiostat running with NOVA 1.8 Software. The electrolyte was purged with N<sub>2</sub> and then pumped through the cell using a peristaltic pump. The measurements were carried out at three different fixed potentials (0.2, 0.4 and 0.6 V vs. RHE). The measurements were run both in 0.5 M H<sub>2</sub>SO<sub>4</sub> and 0.5 M H<sub>2</sub>SO<sub>4</sub> + 0.5 M CH<sub>3</sub>CH<sub>2</sub>OH. Details of the procedure can be found in the SI. X-ray adsorption (XAS) measurements for the fresh samples were recorded on beamline B18 at Diamond Light Source (UK) with ring energy of 3 GeV and a current of 300 mA. The monochromator used was Si(311) crystals operating in Quick EXAFS (QEXAFS) mode. The measurements were carried out in fluorescence mode at the Pt L<sub>3</sub> (11,564 eV) and Sn K (29,200 eV) absorption edges at 298 K using a 9-element Ge detector. XAS measurements for the aged samples were recorded on beamline CLAES5 at ALBA synchrotron light source (Spain). Calibration of the monochromator was carried out using a Pt foil and Sn foil previously to the nanoparticle measurements at the respective absorption edge.

*Ex-situ* XAS measurements were also recorded in transmission mode on beamline B18 at Diamond Light Source (UK) and details can be found in the SI.

The acquired data was processed and analyzed using the programs Athena and Artemis [23], respectively, which implement the FEFF6 and IFEFFIT codes [24]. Fits were carried out using a *k* range of 3–16 Å<sup>-1</sup> and an *R* range of 1.4–4.2 Å at the Pt L<sub>3</sub> edge, and 3–10 Å<sup>-1</sup> and 1.1–3.2 Å at the Sn K edge, with multiple *k* weightings of 1, 2 and 3. Different FEFF inputs were used in these fits depending on the materials. An alloy 3:1 Pt:Sn model was created based on [25,26] using the lattice parameters obtained from the XRD analysis.

#### 2.5. *In situ* IR measurements

Electrochemical *in situ* subtractive normalized interfacial Fourier transform infrared spectroscopy (SNIFTIRS) experiments were carried out on a Thermo Nicolet 8700 (Nicolet, Madison, WI) spectrometer equipped with a custom-made external tabletop optical mount and an MCT-A detector. A custom made glass-filled Teflon® electrochemical cell with a polycrystalline gold disc electrode was coupled to the set-up

to acquire *in situ* IR spectra. The cell was connected to a Jaisle IMP88 Potentiostat (Germany) controlled by the computer *via* a digital to analog converter (Agilent USB AD/DA converter). The IR window was a 1 in. (~25 mm) CaF<sub>2</sub> equilateral prism (Harrick Scientific Technology, Pleasantville, NY). Prior to the assembly of the spectroelectrochemical cell, the gold electrode was modified with the catalysts by depositing 30 μL of catalyst ink prepared with 2 mg catalyst, 15 μL Nafion solution (10.85 wt%) and 500 μL water. A Pt wire and an Ag/AgCl (3 M KCl) were used as counter and reference electrodes, respectively. The cell was filled with 0.1 M HClO<sub>4</sub> solution and fifty conditioning CVs were run between 0.05 and 0.6 V vs. RHE at 0.2 V s<sup>-1</sup> to clean the surface. Three further cycles were recorded at 0.010 V s<sup>-1</sup> to ensure that the electrode was stable. Then, the base electrolyte was exchanged with a 0.5 M CH<sub>3</sub>CH<sub>2</sub>OH + 0.1 M HClO<sub>4</sub> solution for the IR measurements. Prior to the IR measurements, the thickness of the thin layer of electrolyte between the optical window and the gold electrode was set to 7.5–8.2 μm, with the value determined by comparing the experimental reflectivity spectrum of the thin layer cell attenuated by the layer of the solvent to the reflectivity curve calculated from the optical constants of the cell constituents [27,28]. Potential loops were performed for each experiment, varying the potential between 0.05 and 1 V vs. RHE with a 0.05 V step. Each potential step comprises an equilibration time of 1 min followed by the acquisition of the spectrum by averaging 200 scans at 4 cm<sup>-1</sup> resolution. For each sample, a spectrum was measured at 0.05 V and taken as reference (R<sub>0</sub>), since no ethanol oxidation occurs at this potential. The spectra presented in the text correspond to the ratio between the spectrum at the specific potential and the reference one. In SNIFTIRS spectra usually there are bands in both up and down direction with respect to the baseline. Taking R<sub>0</sub> as the reflectance in the reference spectrum and R the sample spectrum reflectance, positive bands (R<sub>0</sub> > R) correspond to consumption of species and negative bands (R<sub>0</sub> < R) correspond to formation of new species.

### 3. Results

Three nanoparticle Pt-Sn catalysts with different structure and composition were prepared: two Pt-Sn alloys with Pt:Sn atomic ratio of 3:1 (Pt<sub>3</sub>Sn<sub>1</sub>/C) and 1:1 (Pt<sub>1</sub>Sn<sub>1</sub>/C), and a one monolayer Sn modified Pt catalyst (Sn/Pt/C). The commercial Pt/C catalyst from Johnson Matthey (JM) was also included in this study as reference.

The bulk composition of the catalysts was determined by using SEM-EDX and the results are reported in Table S1. The metal loading was around 19.5–25.9 wt%, depending on the type of material. In all cases, except for the Sn/Pt/C, the amount of Sn was slightly lower than the nominal one.

The distribution and size of the metal particles deposited on the carbon support were studied by TEM and representative images for all the Pt-Sn catalysts are exhibited in Fig. S1. All catalysts show a narrow particle size distribution. TEM images of the Sn/Pt/C sample show well dispersed nanoparticles on the support. In contrast, the Pt-Sn alloy samples show different degrees of agglomeration, which is most evident for the Pt<sub>3</sub>Sn<sub>1</sub>/C material (Fig. S1b).

The local composition and architecture of the Sn/Pt/C and Pt<sub>3</sub>Sn<sub>1</sub>/C samples were investigated by using an EDS probe in the STEM mode (Fig. 1). Multiple single-particle EDS analyses of both samples confirmed the bimetallic nature of the particles. In both samples, only a few monometallic Pt particles were observed and no monometallic Sn particles were detected. In order to confirm the core-shell and alloy nanostructures, STEM-EDS line spectra were recorded. The composition profile obtained for the Sn/Pt/C sample show that the distribution of Sn reaches a maximum at the edge of the particles (shell) and a minimum at the center of the particle, whereas Pt reaches a maximum concentration at the center of the particles (core). This indicates that Sn was deposited on the surface of the Pt nanoparticles. On the other hand, the composition profile for the Pt<sub>3</sub>Sn<sub>1</sub>/C sample indicates that the distribution profile of both metals is the same, confirming the formation of

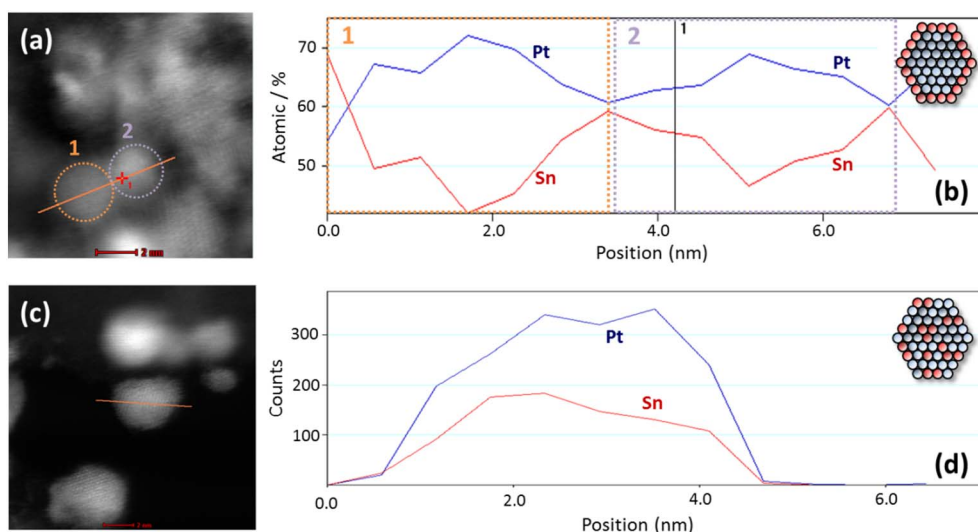


Fig. 1. HAADF atomic-resolution images (a,c) and corresponding STEM-EDS spectra (b,d) along the line in the image for the Sn/Pt/C (a,b) and Pt<sub>3</sub>Sn<sub>1</sub>/C (c,d) samples. The insets in (b) and (d) show the schema of the Pt-Sn nanostructures where blue and red circles represent Pt and Sn atoms, respectively. (For interpretation of the references to color in this figure legend, the reader is referred to the web version of this article.)

the alloy.

The effect of Sn addition on the structural and crystallographic properties of Pt was studied by XRD (Fig. 2a). The broad diffraction peak observed at  $2\theta = 22.5^\circ$  in all the samples is attributed to the sample holder, which overlaps the peak of the (002) plane of the carbon support at  $2\theta = 22.7^\circ$ . The two alloys show the typical features of the fcc structure of Pt. However, the diffraction peaks are slightly shifted to lower  $2\theta$  values, confirming the incorporation of Sn into the fcc structure of Pt. In the literature, a shift of the Pt fcc structure peaks to lower  $2\theta$  values has been observed with the increase of the Sn content [11,29,30]. However, in this case the peaks of the Pt fcc structure for the Pt<sub>1</sub>Sn<sub>1</sub>/C sample are broad and have low intensity, which is attributed to a diminishment of the Pt crystallinity due to the large Sn content – this complicates accurate determination of the peak position shift. In fact, for this sample, additional peaks associated with the (110), (101), (211), (220) and (202) planes of SnO<sub>2</sub> can be observed, indicating the poor grade of alloying between Pt and Sn, which is only 66.8% versus 92.6% for the Pt<sub>3</sub>Sn<sub>1</sub>/C sample. Pt<sub>1</sub>Sn<sub>1</sub> does not show the peaks associated with the hcp phase expected for a Pt<sub>1</sub>Sn<sub>1</sub> alloy, indicating that this sample might be a mixture of the fcc phase with a considerable amount of Sn not alloyed to Pt and segregated to the surface forming SnO<sub>2</sub>. In contrast, no peaks related to Sn or its oxides are observed for the Pt<sub>3</sub>Sn<sub>1</sub>/C sample. Due to the incorporation of Sn into the fcc structure of Pt, an expansion of the lattice cell is expected since the atomic radius of Sn (1.61 Å) is larger than that of Pt (1.39 Å). In agreement with this, the lattice parameter of the Pt-Sn alloy samples

is greater than that of Pt/C-JM (3.9175 Å) reference and increases with the amount of Sn to 3.9776 Å and 4.0260 Å for Pt<sub>3</sub>Sn<sub>1</sub>/C and Pt<sub>1</sub>Sn<sub>1</sub>/C, respectively. The crystallite size was calculated using the Scherrer equation. Pt<sub>3</sub>Sn<sub>1</sub>/C and Pt<sub>1</sub>Sn<sub>1</sub>/C materials have an average crystallite size of 3.4 and 3.3 nm, respectively. These values are in good agreement with those observed by TEM (Fig. S1).

Sn/Pt/C shows the characteristic peaks of the fcc structure of Pt. In this case, no shifts in the peaks are observed, but the peaks associated to the (110), (101), (211), (220) and (202) planes of SnO<sub>2</sub> are observed, which is in agreement with the fact that Sn was not incorporated into the structure of Pt but deposited on its surface as tin oxide, as seen by STEM-EDS. The fact that Sn was not incorporated into the Pt structure is also deduced from the lattice parameter (3.9196 Å), which is very similar to that of Pt/C-JM (3.9175 Å). The average crystallite size for this material is 4.0 nm, the same as that for the commercial 20 wt% Pt/C-JM catalyst used in its synthesis, and the amount of Sn alloyed is only 8%.

The effect of Sn on the electronic properties of Pt, as well as the surface composition, was determined by XPS. Fig. 2b shows the Pt 4f and Sn 3d XPS spectra for the Pt-Sn catalysts and the commercial Pt/C from JM; the corresponding analysis of both regions is reported in Table S2. The Pt 4f lines contain two peaks, which correspond to Pt 4f<sub>7/2</sub> and 4f<sub>5/2</sub> states from the spin-orbital splitting. Each peak was deconvoluted using three different chemically shifted components (Pt<sup>0</sup>, Pt<sup>2+</sup> and Pt<sup>4+</sup>) to identify the predominant oxidation state of Pt. As seen in Table S2, Pt<sup>0</sup> is the predominant oxidation state in all the Pt-Sn catalysts

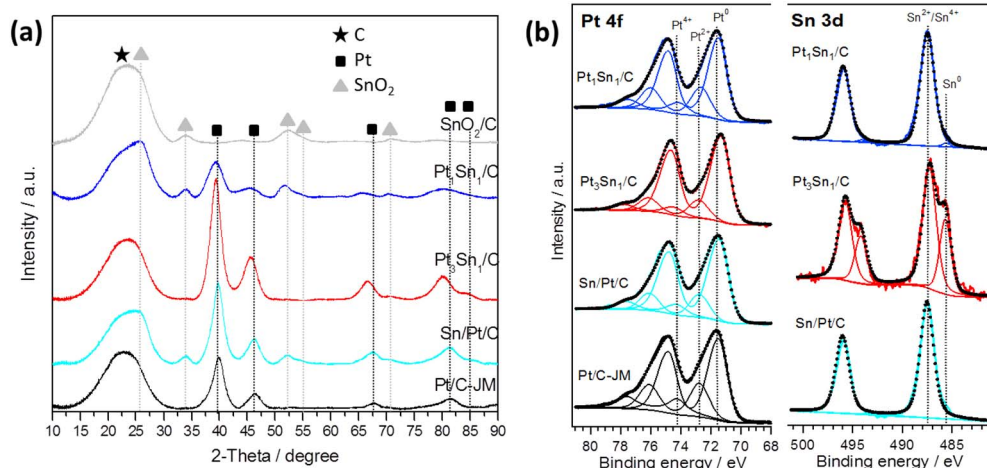


Fig. 2. XRD diffraction patterns (left) and photoemission spectra (right) for the commercial Pt/C-JM, Sn/Pt/C, Pt<sub>1</sub>Sn<sub>1</sub>/C, and Pt<sub>3</sub>Sn<sub>1</sub>/C catalysts. In the right panel, the Pt 4f and Sn 3d regions as well as the corresponding chemical shifted components are shown.

(around 68–78%). However, all samples present a variable amount of oxidized species, deduced from the Pt 4f<sub>7/2</sub> peaks at 72.7–74.5 eV. The presence of Pt oxide phases in all the samples can be attributed to air exposure. This result is explained in more detail with the *ex situ* EXAFS analysis (see *Ex situ* XAS measurements Section in SI).

A shift in the binding energy of the Pt core level to lower energies, compared to those for Pt/C, is observed for the Pt<sub>3</sub>Sn<sub>1</sub>/C alloy catalyst (Table S2). This effect may be caused by electronegativity differences of Pt and Sn, and could indicate a charge transfer from Sn, which is less electronegative, to Pt, which is more electronegative, indicating that there is an electronic modification of Pt. For the Pt<sub>1</sub>Sn<sub>1</sub>/C sample, however, this effect is not observed, which could be attributed to the poor extent of alloying between Pt and Sn. For the Pt sample modified with Sn, the binding energies are the same as those for the commercial Pt/C, indicating that, in this case, Sn does not modify the electronic environment of Pt. The electronic effect of the addition of Sn in the different nanostructures was also confirmed by X-ray absorption near edge spectroscopy (XANES) data analysis, and it is explained in the SI (Fig. S3).

The Sn 3d XPS spectra also show two peaks, which correspond to Sn 3d<sub>5/2</sub> and 3d<sub>3/2</sub> states. In this case, the peaks were deconvoluted into two components, one around 487.5 eV attributed to Sn<sup>2+</sup> and Sn<sup>4+</sup> species and the other one around 485.6 eV corresponding to Sn<sup>0</sup> (considered only for the alloy materials). It should be noted that it is not possible to distinguish between Sn<sup>2+</sup> and Sn<sup>4+</sup> by this technique, as their binding energies are too close. As seen in Fig. 2b, Sn is predominantly oxidized in all the samples, which is in agreement with other reports in the literature [10,11,29,31] and can be attributed to the strong affinity of Sn towards oxygen. In the Pt<sub>3</sub>Sn<sub>1</sub>/C sample, a well-defined shoulder at 485.6 eV is observed, indicating that the presence of Sn<sup>0</sup> is significant in this material, which is attributed to the formation of the Pt-Sn alloy. In the fit of the Pt<sub>1</sub>Sn<sub>1</sub>/C sample, it was necessary also to include the peak corresponding to Sn<sup>0</sup> in order to obtain the best fit.

The surface Pt/Sn atomic ratio was calculated from the Pt 4f and Sn 3d peak areas, taking into account the corresponding sensitivity factors (Table S2). In all the Pt-Sn/C samples, the Pt/Sn ratio in the surface (XPS) is lower than that in the bulk (EDX). For the Pt sample modified with Sn, this is justified by the presence of Sn only on the surface of the Pt nanoparticles. However, in the case of the alloy samples, it indicates a surface Sn enrichment. This behaviour has already been described in the literature and it is explained by the lower surface free energy of Sn, respect to Pt, causing the migration of Sn from bulk to the surface [29].

The stability of these materials under electrochemical conditions over the applied potential (potential range = 0.2–0.6 V vs. RHE) and the effects of ethanol on the structures were determined by using *in situ* EXAFS measurements. The parameters extracted from the EXAFS spectra fits for the fresh samples are reported in Tables 1, 2 and S4, whilst the Fourier transformed EXAFS spectra and the corresponding *k*-space spectra are depicted in Figs. S4 and S5.

Comparing the structural parameters determined from the *ex situ* and *in situ* EXAFS measurements, attention is drawn to the disappearance of the Pt oxide (Pt-O<sub>1</sub> path) under electrochemical conditions. This result is expected since the potentials investigated are below the potential at which platinum oxide starts to be formed. The reduction of Pt oxide under working conditions is evident from the XANES spectra recorded at 0.4 V (double layer region) at the Pt L<sub>3</sub> edge (Fig. S6a). A significant reduction of the white line (WL) intensity is observed, compared with the *ex situ* XANES data reported in Fig. S3a. In the case of Pt/C-JM and Sn/Pt/C, the intensity of the WL is the same as that of the Pt foil, indicating that Pt mainly exists as metallic phase. The decrease of the WL intensity observed for the Pt-Sn alloys compared to the Pt foil, which becomes more significant with the increase of the alloy degree, confirms that the modification of the electronic structure of Pt due to the electron donation from Sn is maintained under working conditions. The reduction of Pt is also accompanied by other changes in

the fitted models that will be described below for each sample.

The commercial Pt/C-JM sample was measured under the same conditions as a reference. As mentioned above, the Pt oxide in the surface of the Pt NPs due to contact with air is reduced under the electrochemical conditions (Table S4). The reduction of Pt results in an increase of the Pt atoms in the first coordination shell from 5.1 to 9.07 (at 0.4 V vs. RHE, double layer region). The applied potential seems to not have any significant influence on the Pt structure in the 0.2–0.6 V potential range, since there is no variation of the coordination number, the Pt–Pt bond length or the disorder ( $\sigma^2$ ). The slight variations observed are within the error of the fits. The adsorption of ethanol does not cause changes in the coordination distance or the disorder, and therefore it can be said that the presence of ethanol does not alter the Pt structure.

The analysis of the Sn/Pt/C at the Pt L<sub>3</sub> edge indicates that Pt is reduced under these electrochemical conditions, as observed for the Pt/C-JM sample, which is reflected in the increase of the Pt atoms in the first coordination shell. It was not possible to fit the Pt-Sn shell because the amount of Pt atoms with a Sn neighbour is too small to be reliably fitted, as described in the SI for the *ex situ* measurements. The analysis at the Sn K edge suggests that the SnO<sub>2</sub> shell is very stable and it is not reduced under electrochemical conditions due to the high affinity of Sn towards oxygen (see also Fig. S6b). Varying the potential does not result in changes of the coordination number (N) or coordination distances (R), indicating that the Sn/Pt nanostructure is stable under operating conditions. The introduction of ethanol in the cell does not cause variation of the structural parameters at 0.2 and 0.4 V at the Pt edge. However, an increase of the Sn–Sn bond distance from 3.223 to 3.239 Å and the decrease of the Sn–O coordination number from 5.28 to 4.81 are observed at 0.6 V in the presence of ethanol. This could indicate a slight reduction of the SnO<sub>2</sub> layer due to the adsorption of ethanol.

For the Pt<sub>3</sub>Sn/C sample, a slight increase of the Pt-Sn interactions at the Pt L<sub>3</sub> edge is observed when increasing the potential, which has been previously attributed to a change in the morphology, from more spherical at low potentials to a more raft-like at higher potentials [32]. In that work, the samples were only analyzed at the Pt L<sub>3</sub> edge. Analysing the samples at the Sn K edge, a slight increase of the Sn-Pt interactions, as well as an increase of the Sn-O ones, is also observed. In presence of ethanol, the migration of the Sn atoms into the NPs could take place, which may be attributed to a higher affinity of Pt towards ethanol. These morphological changes are evidenced by a decrease of the N<sub>Pt-Pt</sub> and increase of N<sub>Pt-Sn</sub> with an increase of the R<sub>Pt-Pt</sub> and a decrease of R<sub>Pt-Sn</sub>. In the presence of ethanol, a slight decrease in the number of Sn-O interactions is also observed for this sample, which is interpreted as a slight reduction of the SnO<sub>2</sub> layer due to the adsorption of ethanol, as for the Sn/Pt/C sample. However, despite the small changes, it can be concluded that both nanostructures are stable in the potential range studied and in presence of ethanol.

Once the stability of the Pt-Sn nanostructures under EOR conditions was confirmed, the EOR activities were established using cyclic voltammetry. Fig. 3 shows the activity of the different Pt-Sn materials and the commercial Pt/C. It can be clearly seen that the addition of Sn results in an approximately 0.2 V shift of the onset potential to more negative potentials and in the increase of the current densities, compared to those obtained with the commercial Pt/C-JM. This effect is attributed to the fact that Sn promotes the water activation at lower potentials than Pt (see CO-stripping CVs in Fig. S7), incorporating oxidant species (OH<sub>ads</sub>) to the surface that helps to oxidize ethanol. This result is consistent with the fact that the ethanol oxidation starts at around 0.6 V on Pt NPs, a potential at which OH<sub>ads</sub> species are present on the NP surface [33]. In the literature, the better performance of the Pt-Sn alloys in the electrooxidation of ethanol, both in terms of current density at a given potential and onset potential, has also been attributed both to the expansion of the lattice parameter of Pt (seen by XRD), which could catalyse the cleavage of the C–C bond, and to the

**Table 1**

Structural parameters obtained for the Sn/Pt/C catalyst from fitting the Pt L<sub>3</sub> and Sn K edges EXAFS data acquired under potential control in 0.5 M H<sub>2</sub>SO<sub>4</sub> and in 0.5 M CH<sub>3</sub>CH<sub>2</sub>OH + 0.5 M H<sub>2</sub>SO<sub>4</sub>.

Electrolyte	Potential vs. RHE	Shell	N	R/Å	$\sigma^2 \times 10^4/\text{Å}^2$	$\Delta E_0/\text{eV}$	R <sub>f</sub>
0.5 M H <sub>2</sub> SO <sub>4</sub>	0.2 V	Pt-Pt <sub>1</sub>	8.92 ± 0.29	2.743 ± 0.001	55 ± 1	7.4 ± 0.3	0.005
		Sn-Sn	1.65 ± 0.91	3.213 ± 0.019	56 ± 41	5.0 ± 0.9	0.011
		Sn-O	5.36 ± 0.38	2.053 ± 0.007	32 ± 9		
	0.4 V	Pt-Pt <sub>1</sub>	9.10 ± 0.27	2.744 ± 0.001	57 ± 1	7.3 ± 0.3	0.003
		Sn-Sn	1.47 ± 0.74	3.214 ± 0.015	27 ± 31	4.3 ± 0.9	0.012
		Sn-O	5.43 ± 0.40	2.056 ± 0.007	35 ± 9		
	0.6 V	Pt-Pt <sub>1</sub>	8.90 ± 0.33	2.744 ± 0.002	56 ± 2	7.2 ± 0.3	0.003
		Sn-Sn	1.69 ± 1.00	3.222 ± 0.021	58 ± 46	4.3 ± 0.9	0.012
		Sn-O	5.39 ± 0.40	2.053 ± 0.007	29 ± 9		
0.5 M H <sub>2</sub> SO <sub>4</sub> + 0.5 M EtOH	0.2 V	Pt-Pt <sub>1</sub>	9.07 ± 0.30	2.747 ± 0.002	57 ± 2	7.0 ± 0.5	0.003
		Sn-Sn	1.72 ± 0.82	3.226 ± 0.017	54 ± 35	5.2 ± 0.9	0.010
		Sn-O	5.32 ± 0.36	2.053 ± 0.007	37 ± 9		
	0.4 V	Pt-Pt <sub>1</sub>	9.28 ± 0.27	2.747 ± 0.001	58 ± 1	7.0 ± 0.6	0.005
		Sn-Sn	1.83 ± 0.85	3.223 ± 0.017	58 ± 35	5.1 ± 0.8	0.010
		Sn-O	5.28 ± 0.36	2.053 ± 0.006	34 ± 8		
	0.6 V	Pt-Pt <sub>1</sub>	9.15 ± 0.43	2.747 ± 0.002	58 ± 2	6.9 ± 0.4	0.006
		Sn-Sn	1.73 ± 1.28	3.239 ± 0.008	79 ± 66	5.0 ± 1.0	0.019
		Sn-O	4.81 ± 0.40	2.052 ± 0.009	21 ± 10		

electronic effect that could result in a weaker bond between Pt and carbon atoms, preventing and/or reducing the poisoning by intermediate species [33,34]. Therefore, both the structural and electronic effect could explain the higher current densities obtained with the two Pt-Sn alloys (Pt<sub>3</sub>Sn/C and Pt<sub>1</sub>Sn<sub>1</sub>/C) than with the Sn modified Pt surface. Recently, it has been demonstrated that Pt-Sn materials promote the partial oxidation of ethanol to acetaldehyde and acetic acid [7,35], suggesting that the higher currents obtained during the CV measurements are due to the production of these partial oxidation products and not the complete oxidation of ethanol to CO<sub>2</sub>.

In order to determine the origin of variation in EOR activity observed in Fig. 3 and any differences in selectivity of the catalysts, the EOR at the different nanostructures was followed *in situ* by FTIR, as shown in Fig. 4. Similar adsorbed species can be observed during the electrooxidation of ethanol on all the Pt-Sn materials investigated and on the commercial Pt/C (see Fig. 4a–d). The band observed at ca. 2342 cm<sup>-1</sup> is attributed to the formation of CO<sub>2</sub> and, therefore, to the complete oxidation of ethanol [36,37]. The band at ca. 1715 cm<sup>-1</sup>

corresponds to the C–O stretch of the carbonyl group in both acetaldehyde and acetic acid [37], whereas the band at 1280 cm<sup>-1</sup> corresponds to the C–OH stretching in the acetic acid [38]. The latter band will be used to quantify the acetic acid formed, since it can be attributed unequivocally to this product. However, no bands can be exclusively ascribed to the formation of acetaldehyde. The broad band centred at ca. 1623 cm<sup>-1</sup> is associated with the consumption of water during the electrooxidation of ethanol, and the positive bands at ~2900 cm<sup>-1</sup> to the loss of ethanol in the thin layer [37]. It is noteworthy that the bands associated with linear (2050 cm<sup>-1</sup>, CO<sub>L</sub>) and bridge (1836 cm<sup>-1</sup>, CO<sub>B</sub>) bonded CO were not observed for most of the catalysts [39]. Only the band characteristic of linear bonded CO was observed on the Pt<sub>1</sub>Sn<sub>1</sub>/C sample at potentials as low as 0.17 V (Fig. 4d).

Although the species adsorbed on the different Pt-Sn materials were similar, the product distributions varied significantly with the different Pt-Sn nanoarchitectures as illustrated in Fig. 4e–h, which show the amount of CO<sub>2</sub> and acetic acid formed as a function of the applied potential. In agreement with the literature, both the Pt-Sn alloys

**Table 2**

Structural parameters obtained for the Pt<sub>3</sub>Sn<sub>1</sub>/C catalyst from fitting simultaneously the Pt L<sub>3</sub> and Sn K edges EXAFS data acquired under potential control in 0.5 M H<sub>2</sub>SO<sub>4</sub> and in 0.5 M CH<sub>3</sub>CH<sub>2</sub>OH + 0.5 M H<sub>2</sub>SO<sub>4</sub>.

Electrolyte	Potential vs. RHE	Shell	N	R/Å	$\sigma^2 \times 10^4/\text{Å}^2$	$\Delta E_0/\text{eV}$	R <sub>f</sub>
0.5 M H <sub>2</sub> SO <sub>4</sub>	0.2 V	Pt-Pt	8.96 ± 0.38	2.757 ± 0.003	67 ± 2	5.5 ± 0.5	0.007
		Pt-Sn	1.14 ± 0.31	2.796 ± 0.012	102 ± 24		
		Sn-Pt	5.22 ± 1.37	2.796 ± 0.012	102 ± 24	3.5 ± 1.5	
	0.4 V	Sn-O	3.55 ± 0.42	2.052 ± 0.015	47 ± 17		
		Pt-Pt	8.86 ± 0.39	2.762 ± 0.003	67 ± 3	6.2 ± 0.5	0.007
		Pt-Sn	1.27 ± 0.30	2.800 ± 0.009	96 ± 20		
	0.6 V	Sn-Pt	5.25 ± 1.23	2.800 ± 0.009	96 ± 20	3.4 ± 1.3	
		Sn-O	3.73 ± 0.43	2.051 ± 0.011	59 ± 17		
		Pt-Pt	8.98 ± 0.39	2.758 ± 0.003	70 ± 3	6.0 ± 0.5	0.008
0.5 M H <sub>2</sub> SO <sub>4</sub> + 0.5 M EtOH	0.2 V	Pt-Sn	1.52 ± 0.41	2.805 ± 0.011	115 ± 29		
		Sn-Pt	5.42 ± 1.82	2.805 ± 0.011	115 ± 29	3.0 ± 1.7	
		Sn-O	3.78 ± 0.61	2.047 ± 0.015	49 ± 23		
	0.4 V	Pt-Pt	8.84 ± 0.28	2.756 ± 0.002	65 ± 2	5.2 ± 0.4	0.005
		Pt-Sn	1.15 ± 0.41	2.797 ± 0.014	147 ± 40		
		Sn-Pt	8.30 ± 3.17	2.797 ± 0.014	147 ± 40	2.3 ± 2.0	
	0.6 V	Sn-O	3.23 ± 0.75	2.033 ± 0.017	42 ± 30		
		Pt-Pt	8.74 ± 0.31	2.761 ± 0.002	65 ± 2	5.6 ± 0.4	0.009
		Pt-Sn	1.22 ± 0.44	2.793 ± 0.015	129 ± 41		
0.6 V	Sn-Pt	6.80 ± 2.98	2.793 ± 0.015	129 ± 41	3.1 ± 2.4		
	Sn-O	3.67 ± 0.93	2.041 ± 0.021	49 ± 35			
	Pt-Pt	8.81 ± 0.65	2.764 ± 0.005	68 ± 5	6.1 ± 0.9	0.013	
0.6 V	Pt-Sn	1.35 ± 0.78	2.784 ± 0.024	119 ± 63			
	Sn-Pt	6.98 ± 4.90	2.784 ± 0.024	119 ± 63	3.8 ± 1.0		
	Sn-O	3.17 ± 1.46	2.030 ± 0.033	39 ± 6			

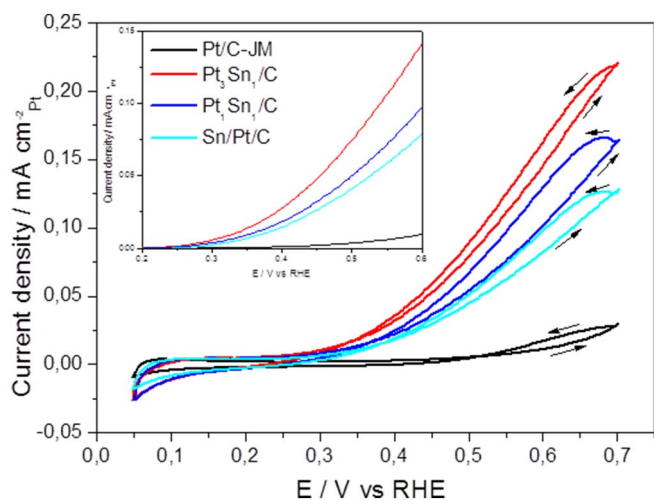


Fig. 3. Cyclic voltammograms in 0.5M H<sub>2</sub>SO<sub>4</sub> + 0.5M CH<sub>3</sub>CH<sub>2</sub>OH obtained at room temperature and at a scan rate of 0.02 V s<sup>-1</sup> for the Pt-Sn/C catalysts and the commercial Pt/C from JM. Inset: enlargement of the onset potential for the ethanol electrooxidation during the forward scan after double layer removal.

produced more acetic acid than CO<sub>2</sub> [20]. Additionally, the acetic acid/CO<sub>2</sub> ratio was found to be greater for Pt<sub>3</sub>Sn<sub>1</sub>/C than Pt<sub>1</sub>Sn<sub>1</sub>/C, thus increasing with the extent of Pt-Sn alloying. In contrast, the Sn modified Pt surface nanostructure was more selective to CO<sub>2</sub>.

Expansion of the lattice parameter of Pt by alloying has been previously suggested to facilitate the C–C bond breaking, improving the selectivity to CO<sub>2</sub> [29,40]. However, such trend in the selectivity to CO<sub>2</sub> with lattice constant was not found for the catalysts in our study. Although, the lattice expansion may contribute to the overall increased current density as shown in Fig. 3, this is not reflected in the *in situ* FTIRS results.

The selectivity to acetic acid formation (reduced selectivity to CO<sub>2</sub>) is attributed to the electronic effect of Sn on the Pt, resulting in weaker adsorption of the intermediates (acetaldehyde and acetic acid), which

desorb easily from the surface of the catalyst not allowing their further oxidation to CO<sub>2</sub>. This effect is most significant for the Pt<sub>3</sub>Sn<sub>1</sub>/C (92.6% alloying) compared to Pt<sub>1</sub>Sn<sub>1</sub>/C (67% alloying). In the case of the Sn/Pt/C catalyst, the deposition of Sn on the surface of Pt NPs did not cause any electronic effect (as observed in the XPS and XANES), implying a stronger adsorption of the intermediates, which allows them to be further oxidized to CO<sub>2</sub>. Our results contradict those of Du et al. who report the differences between alloy and non-alloyed Pt-Sn catalyst in the conversion to CO<sub>2</sub> and attributed these to the composition of the catalysts and not to the crystalline structure [13].

The long-term stability of the nanostructures is also of importance in designing more effective EOR electrocatalysts. The stability was therefore investigated by using *in situ* XAS and post-mortem XPS measurements performed on the samples subjected to an accelerated aging treatment (AAT). The structural and electronic results extracted from the XAS and XPS analysis are reported in Tables 3 and S5 and Figs. S8–S10, whilst the electrochemical data can be found in Fig. S11.

The EXAFS analysis of the Sn modified Pt structure demonstrates the stability of this nanostructure in the potential window studied and precludes significant dissolution of Sn, since no changes in the EXAFS parameters were observed. The stability of Sn was also confirmed by XPS, since the atomic Pt:Sn ratio did not change with the AAT. This result is also supported by the electrochemical data that shows only a slight decrease of the electrochemical surface area, calculated both from the hydrogen UPD region and the CO-stripping peak.

In the case of the Pt<sub>3</sub>Sn<sub>1</sub>/C sample, however, significant changes in the atomic structure are deduced from the EXAFS fit. A significant decrease of the Pt-Sn interactions, accompanied by an increase of the Pt–Sn bond length, suggests the segregation of Sn to the surface with cycling, resulting in the de-alloying of the Pt-Sn nanoparticles. In addition, the increase of the Sn-O coordination number confirms the segregation of the Sn atoms and the formation of a SnO<sub>2</sub> layer at the surface of the nanoparticles (SnO<sub>2</sub>/Pt<sub>3</sub>Sn/C). The XPS results corroborate the de-alloying of the Pt-Sn nanoparticles with the subsequent increase of SnO<sub>2</sub>. The Sn 3d photoemission line shows a decrease of the metal Sn component respect to the as-prepared sample (Figs. 2 and S10, Tables S2 and S5). However, the electronic effect on Pt was preserved

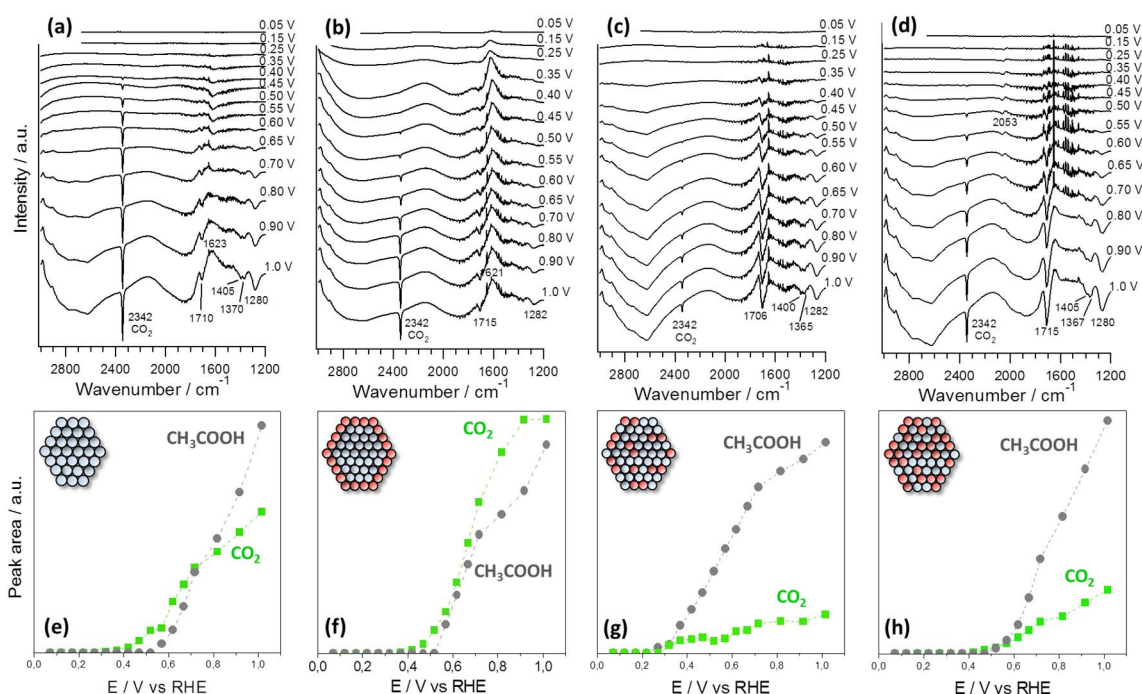


Fig. 4. *In situ* FTIR spectra taken at different potentials in 0.5 M CH<sub>3</sub>CH<sub>2</sub>OH + 0.1 M HClO<sub>4</sub> (upper panels); and normalized areas of the CO<sub>2</sub> (2343 cm<sup>-1</sup>) and acetic acid (1280 cm<sup>-1</sup>) bands as function of the applied potential (bottom panels) for Pt/C-JM (a,e), Sn/Pt/C (b,f), Pt<sub>3</sub>Sn<sub>1</sub>/C (c,g) and Pt<sub>1</sub>Sn<sub>1</sub>/C (d,h) catalysts. The insets in (e)–(h) show the Pt-Sn nanostructures where blue and red circles represent Pt and Sn atoms, respectively.

**Table 3**

Structural parameters obtained for the aged Pt-Sn materials supported on carbon from fitting the Pt L<sub>3</sub> and Sn K edge EXAFS data acquired at 0.2 V in 0.5 M H<sub>2</sub>SO<sub>4</sub>. For the Pt<sub>3</sub>Sn<sub>1</sub>/C sample, both edges were fitted simultaneously.

Sample	Shell	N	R/Å	$\sigma^2 \times 10^4/\text{Å}^2$	$\Delta E_0/\text{eV}$	R <sub>r</sub>
Pt/C-JM	Pt-Pt	9.00 ± 0.86	2.753 ± 0.004	53 ± 5	8.0 ± 0.7	0.020
	Sn/Pt/C	8.82 ± 0.46	2.748 ± 0.005	65 ± 5	6.6 ± 0.5	0.003
Pt <sub>3</sub> Sn <sub>1</sub> /C	Sn-Sn	1.38 ± 0.82	3.213 ± 0.019	41 ± 41	5.6 ± 0.9	0.011
	Sn-O	5.33 ± 0.40	2.048 ± 0.007	37 ± 10		
	Pt-Pt	7.97 ± 0.79	2.759 ± 0.006	57 ± 5	6.2 ± 1.1	0.016
	Pt-Sn	0.57 ± 0.61	2.808 ± 0.012	103 ± 33		
	Sn-Pt	4.61 ± 1.66	2.808 ± 0.012	103 ± 33	3.7 ± 1.4	
	Sn-O	4.14 ± 0.36	2.049 ± 0.010	41 ± 12		

after the AAT, which is evidenced by the shift in the binding energy of the Pt core level to lower energies compared to that of Pt/C and Sn/Pt/C. The electrochemical data shows a significant decrease of the H<sub>UPD</sub> area and the CO-stripping peak in agreement with the segregation of Sn to the surface and the formation of a SnO<sub>2</sub> layer. In addition, during the AAT a redox couple at 0.55/0.8 V associated with Sn appears [7], whereas the reduction peak of Pt at 0.8 V disappears.

However, even after the structural changes suffered by the Pt<sub>3</sub>Sn<sub>1</sub>/C during the AAT, its overall activity (not necessarily CO<sub>2</sub> selectivity as discussed above) is still higher than that of the Sn/Pt/C sample. This suggests that the electronic effects retained after the AAT, confirmed by XANES and XPS, continue to have an important role in describing the activity of this material.

#### 4. Conclusions

Three different Pt-Sn nanostructures, two Pt-Sn alloys with varying extent of alloying and a Sn modified Pt catalyst, were investigated to study the effect of the addition of Sn on the structural and electronic properties of Pt and their relative effects on the overall ethanol electrooxidation activity and selectivity to CO<sub>2</sub> formation. The Pt<sub>3</sub>Sn<sub>1</sub>/C and Pt<sub>1</sub>Sn<sub>1</sub>/C samples are alloys with a heterogeneous composition, with more Sn on the surface than in the bulk of the nanoparticles. Pt<sub>3</sub>Sn<sub>1</sub>/C presented a high grade of crystallinity with a 92.6% of alloying. In contrast, Pt<sub>1</sub>Sn<sub>1</sub>/C showed a more amorphous character that was attributed to the excess of Sn present as SnO<sub>2</sub> at the surface or near to the surface of the alloy particles. The Sn/Pt/C sample consisted of a monolayer of Sn deposited on the Pt nanoparticles forming a core-shell structure. Alloying of Sn with Pt caused an increase in the lattice parameter of Pt and modified the electronic structure, whilst the deposition of Sn on the Pt surface did not modify the Pt lattice parameter nor perturbed its electronic environment.

All the Pt-Sn materials showed higher EOR activity than the commercial Pt/C reference catalyst, both in terms of onset potential and current density, with the Pt-Sn alloys giving the highest yield of ethanol oxidized. *In situ* FTIR was used to determine any effect of the Pt-Sn nanostructure on the products distribution. Our study advanced the detailed understanding of the oxidation of ethanol on PtSn catalysts by showing that the architecture of the nanoparticles affects the selectivity towards CO<sub>2</sub>. On the Pt-Sn alloys, the formation of acetaldehyde and acetic acid was confirmed and related to the weaker adsorption of such products due to the modification of the electronic environment of Pt, which desorb easily from the surface of the catalyst and thus are not completely oxidized to CO<sub>2</sub>. In contrast, on the Sn modified Pt sample, the amount of ethanol completely oxidized to CO<sub>2</sub> increased, indicating that the product distribution can be tuned by the Pt-Sn nanostructure.

Both nanoarchitectures were shown to be retained under working conditions and in presence of ethanol in the 0.2–0.6 V potential window. Following AAT cycles, a segregation of Sn from the bulk to the surface of the Pt-Sn alloy nanoparticles was found, causing Pt-Sn dealloying and formation of a SnO<sub>2</sub> layer on the surface. In contrast, the Sn modified Pt nanostructure was very stable. However, even after the

structural changes suffered by the Pt<sub>3</sub>Sn<sub>1</sub>/C sample, its overall activity outperformed that of the Sn/Pt/C sample, suggesting that the electronic effects of alloying persisted and have an important role in describing the activity of this material.

#### Acknowledgments

L.C. acknowledges support via an EU Marie Curie Intra-European Fellowship under contract no. FP7-PEOPLE-2010-IEF-272632. EJC and LMD acknowledge financial support from CONICET and ANPCyT (Argentina). The authors acknowledge the LMA-INA, UK Catalysis Hub, Diamond Light Source and the ALBA synchrotron light source for offering access to their instruments and expertise and for provision of beamtime (SP8071 and 2012100428). Dr. Giannantonio Cibin, Dr. Andy Dent and Dr. Stephen Parry are acknowledged for the excellent beamline support at the Diamond Light Source and Dr. Laura Simonelli at ALBA Synchrotron Light Source. The data used in this paper can be found in the Southampton University Deposit with DOI: <https://doi.org/10.5258/SOTON/D0294>.

#### Appendix A. Supplementary data

Supplementary data to this article can be found online at <https://doi.org/10.1016/j.jelechem.2017.09.060>.

#### References

- [1] C. Lamy, A. Lima, V. LeRhun, F. Delime, C. Coutanceau, J.-M. Léger, Recent advances in the development of direct alcohol fuel cells (DAFC), *J. Power Sources* 105 (2002) 283–296.
- [2] J.S. Spendelov, A. Wieckowski, Electrocatalysis of oxygen reduction and small alcohol oxidation in alkaline media, *Phys. Chem. Phys.* 9 (2007) 2654–2675.
- [3] H. Igarashi, T. Fujino, Y. Zhu, H. Uchida, M. Watanabe, CO tolerance of Pt alloy electrocatalysts for polymer electrolyte fuel cells and the detoxification mechanism, *Phys. Chem. Phys.* 3 (2001) 306–314.
- [4] L. Colmenares, H. Wang, Z. Jusys, L. Jiang, S. Yan, G.Q. Sun, R.J. Behm, Ethanol oxidation on novel, carbon supported Pt alloy catalysts—model studies under defined diffusion conditions, *Electrochim. Acta* 52 (2006) 221–233.
- [5] H.D. Herrera-Méndez, P. Roquero, M.A. Smit, L.C. Ordóñez, Carbon-supported platinum molybdenum electro-catalysts and their electro-activity toward ethanol oxidation, *Int. J. Electrochem. Sci.* 6 (2011) 4454–4469.
- [6] G. Yang, A.I. Frenkel, D. Su, X. Teng, Enhanced electrokinetics of C–C bond splitting during ethanol oxidation by using a Pt/Rh/Sn catalyst with a partially oxidized Pt and Rh core and a SnO<sub>2</sub> shell, *ChemCatChem* 8 (2016) 1–6.
- [7] J.-M. Jin, T. Sheng, X. Lin, R. Kavanagh, P. Hamer, P. Hu, C. Hardacre, A. Martinez-Bonastre, J. Sharman, D. Thompsett, W.-F. Lin, The origin of high activity but low CO<sub>2</sub> selectivity on binary PtSn in the direct ethanol fuel cell, *Phys. Chem. Chem. Phys.* 16 (2014) 9432–9440.
- [8] A. Kowal, M. Li, M. Shao, K. Sasaki, M.B. Vukmircovic, J. Zhang, N.S. Marinkovic, P. Liu, A.I. Frenkel, R.R. Adzic, Ternary Pt/Rh/SnO<sub>2</sub> electrocatalysts for oxidizing ethanol to CO<sub>2</sub>, *Nat. Mater.* 8 (2009) 325–330.
- [9] B.E. Hayden, M.E. Rendall, O. South, The stability and electro-oxidation of carbon monoxide on model electrocatalysts: Pt(111)–Sn(2 × 2) and Pt(1 1 1)–Sn(√3 × √3)R30°, *J. Mol. Catal. A Chem.* 228 (2005) 55–65.
- [10] E.M. Crabb, R. Marshall, D. Thompsett, Carbon monoxide electro-oxidation properties of carbon-supported PtSn catalysts prepared using surface organometallic chemistry, *J. Electrochem. Soc.* 147 (2000) 4440–4447.
- [11] S. García-Rodríguez, F. Somodi, I. Borbáth, J.L. Margitfalvi, M.A. Peña, J.L.G. Fierro, S. Rojas, Controlled synthesis of Pt-Sn/C fuel cell catalysts with exclusive Sn-Pt interaction. Application in CO and ethanol electrooxidation reactions,

- Appl. Catal. B Environ. 91 (2009) 83–91.
- [12] F.E. Lopez-Suarez, C.T. Carvalho-Filho, A. Bueno-Lopez, J. Arboleda, A. Echavarría, K.I.B. Eguiluz, G.R. Salazar-Banda, Platinum–tin/carbon catalysts for ethanol oxidation: influence of Sn content on the electroactivity and structural characteristics, *Int. J. Hydrog. Energy* 40 (2015) 12674–12686.
- [13] W. Du, G. Yang, E. Wong, N.A. Deskins, A.I. Frenkel, D. Su, X. Teng, Platinum-tin oxide core–shell catalysts for efficient electro-oxidation of ethanol, *J. Am. Chem. Soc.* 136 (2014) 10862–10865.
- [14] S. Alayoglu, A.U. Nilekar, M. Mavrikakis, B. Eichhorn, Ru–Pt core–shell nanoparticles for preferential oxidation of carbon monoxide in hydrogen, *Nat. Mater.* 7 (2008) 333–338.
- [15] S. Alayoglu, B. Eichhorn, Rh–Pt bimetallic catalysts: synthesis, characterization, and catalysis of core–shell, alloy, and monometallic nanoparticles, *J. Am. Chem. Soc.* 130 (2008) 17479–17486.
- [16] R. Parsons, T. VanderNoot, The oxidation of small organic molecules: a survey of recent fuel cell related research, *J. Electroanal. Chem.* 257 (1988) 9–45.
- [17] F. Fievet, J.P. Lagier, B. Blin, Homogeneous and heterogeneous nucleations in the polyol process for the preparation of micron and submicron size metal particles, *Solid State Ionics* 32–33 (1989) 198–205.
- [18] J.-H. Zhou, J.-P. He, Y.-J. Ji, W.-J. Dang, X.-L. Liu, G.-W. Zhao, C.-X. Zhang, J.-S. Zhao, Q.-B. Fu, H.-P. Hu, CTAB assisted microwave synthesis of ordered mesoporous carbon supported Pt nanoparticles for hydrogen electro-oxidation, *Electrochim. Acta* 52 (2007) 4691–4695.
- [19] D.L. Boxall, C.M. Lukehart, Rapid synthesis of Pt or Pd/Carbon nanocomposites using microwave irradiation, *Chem. Mater.* 13 (2001) 806–810.
- [20] W. Li, W. Zhou, H. Li, Z. Zhou, B. Zhou, G. Sun, Q. Xin, Nano-structured Pt–Fe/C as cathode catalyst in direct methanol fuel cell, *Electrochim. Acta* 49 (2004) 1045–1055.
- [21] S. Kim, S.-J. Park, Effect of acid/base treatment to carbon blacks on preparation of carbon-supported platinum nanoclusters, *Electrochim. Acta* 52 (2007) 3013–3021.
- [22] A.M. Wise, P.W. Richardson, S.W.T. Price, G. Chouhelamane, L. Cavillo, P.J. Hendra, M.F. Toney, A.E. Russell, Inhibitive effect of Pt on Pd-hydride formation of Pd@Pt core-shell electrocatalysts: an in situ EXAFS and XRD study, *Electrochim. Acta*, (under revision).
- [23] B. Ravel, M. Newville, ATHENA, ARTEMIS, HEPHAESTUS: data analysis for X-ray absorption spectroscopy using IFEFFIT, *J. Synchrotron Radiat.* 12 (2005) 537–541.
- [24] M. Newville, EXAFS analysis using FEFF and FEFFIT, *J. Synchrotron Radiat.* 8 (2001) 96–100.
- [25] W. Zhou, L. Liu, B. Li, P. Wu, Q. Song, Structural, elastic and electronic properties of intermetallics in the Pt–Sn system: a density functional investigation, *Comput. Mater. Sci.* 46 (2009) 921–931.
- [26] X. Wang, L. Altmann, J. Stöver, V. Zielasek, M. Bäumer, K. Al-Shamery, H. Borchert, J. Parisi, J. Kolny-Olesiak, Pt/Sn intermetallic, core/shell and alloy nanoparticles: colloidal synthesis and structural control, *Chem. Mater.* 25 (2013) 1400–1407.
- [27] V. Zamylny, J. Lipkowski, In *Advances in Electrochemical Science and Engineering*, Vol. 9 WILEY, Weinheim, 2006.
- [28] V. Zamylny, I. Zawisza, J. Lipkowski, PM FTIRAS studies of potential-controlled transformations of a monolayer and a bilayer of 4-pentadecylpyridine, a model surfactant, adsorbed on a Au(111) electrode surface, *Langmuir* 19 (2003) 132–145.
- [29] J.H. Kim, S.M. Choi, S.H. Nam, M.H. Seo, S.H. Choi, W.B. Kim, Influence of Sn content on PtSn/C catalysts for electrooxidation of C1–C3 alcohols: synthesis, characterization, and electrocatalytic activity, *Appl. Catal. B Environ.* 82 (2008) 89–102.
- [30] J.M. Sieben, M.M.E. Duarte, Nanostructured Pt and Pt–Sn catalysts supported on oxidized carbon nanotubes for ethanol and ethylene glycol electro-oxidation, *Int. J. Hydrog. Energy* 36 (2011) 3313–3321.
- [31] G. Li, P.G. Pickup, Decoration of carbon-supported Pt catalysts with Sn to promote electro-oxidation of ethanol, *J. Power Sources* 173 (2007) 121–129.
- [32] S. Mukerjee, J. Mcbreen, An in situ X-ray absorption spectroscopy investigation of the effect of Sn additions to carbon-supported Pt electrocatalysts: part I, *J. Electrochem. Soc.* 146 (1999) 600–606.
- [33] S.C. Zignani, E.R. Gonzalez, V. Baglio, S. Siracusano, A.S. Aricò, Investigation of a Pt<sub>3</sub>Sn/C electro-catalyst in a direct ethanol fuel cell operating at low temperatures for portable applications, *Int. J. Electrochem. Sci.* 7 (2012) 3155–3166.
- [34] T.S. Almeida, K.B. Kokoh, A.R. De Andrade, Effect of Ni on Pt/C and PtSn/C prepared by the Pechini method, *Int. J. Hydrog. Energy* 36 (2011) 3803–3810.
- [35] J.M.S. Ayoub, R.F.B. De Souza, J.C.M. Silva, R.M. Piasentin, E.V. Spinacé, M.C. Santos, A.O. Neto, Ethanol electro-oxidation on PtSn/C-ATO electrocatalysts, *Int. J. Electrochem. Sci.* 7 (2012) 11351–11362.
- [36] V. Del Colle, J. Souza-Garcia, G. Tremiliosi-Filho, E. Herrero, J.M. Feliu, Electrochemical and spectroscopic studies of ethanoloxidation on Pt stepped surfaces modified by tin adatoms, *Phys. Chem. Chem. Phys.* 13 (2011) 12163–12172.
- [37] F.C. Simoes, D.M. dos Anjos, F. Vigier, J.-M. Léger, F. Hahn, C. Coutanceau, E.R. Gonzalez, G. Tremiliosi-Filho, A.R. de Andrade, P. Olivi, K.B. Kokoh, Electroactivity of tin modified platinum electrodes for ethanol electrooxidation, *J. Power Sources* 167 (2007) 1–10.
- [38] R.F.B. De Souza, L.S. Parreira, J.C.M. Silva, F.C. Simoes, M.L. Calegario, M.J. Giz, C.A. Camara, A.O. Neto, M.C. Santos, PtSnCe/C electrocatalysts for ethanol oxidation: DEFC and FTIR “in-situ” studies, *Int. J. Hydrog. Energy* 36 (2011) 11519–11527.
- [39] M.H. Shao, R.R. Adzic, Electrooxidation of ethanol on a Pt electrode in acid solutions: in situ ATR-SEIRAS study, *Electrochim. Acta* 50 (2005) 2415–2422.
- [40] W.J. Zhou, S.Q. Song, W.Z. Li, Z.H. Zhou, G.Q. Sun, Q. Xina, S. Douvartzides, P. Tsiakaras, Direct ethanol fuel cells based on PtSn anodes: the effect of Sn content on the fuel cell performance, *J. Power Sources* 140 (2008) 50–58.